1D generalized time dependent non Newtonian blood flow model

Arthur R. Ghigo, Pierre-Yves Lagrée, Jose-Maria Fullana

A 1D generalized time-dependent non-Newtonian blood flow model

A. R. Ghigo[a], P. -Y. Lagrée[a], J. -M. Fullana[a,*]

[a]*Sorbonne Université, CNRS and UPMC Université Paris 06, UMR 7190, Institut Jean Le Rond ∂'Alembert, 4 place Jussieu, Boîte 162, 75005 Paris, FRANCE*

Abstract

Blood pulsatility, aneurysms, stenoses and general low shear stress hemodynamics lead to non-Newtonian blood effects which generate local changes in the space-time evolution of the blood pressure, flow rate and cross-sectional area of elastic vessels. Even though these local changes are known to cause global unexpected hemodynamical behaviors, all one-dimensional (1D) blood flow models are built under the Newtonian fluid hypothesis.

In this work, we present a 1D generalized time-dependent non-Newtonian blood flow model able to describe local space-time variations of the viscous behavior of blood. The rheological model is based on a simplified Maxwell viscoelastic equation for the shear stress with structural dependent coefficients. We compare the numerical predictions of the 1D model to experimental rheological data available in the literature. Specifically, we explore three well documented shear stress protocols and we show that the results predicted by the 1D non-Newtonian model in a single artery accurately compare, both qualitatively and quantitatively, to the time evolution of the shear stress measured using a rheometer. We then use the 1D non-Newtonian model to compute the flow in idealized healthy and pathological symmetric and asymmetric networks of increasing size. We show that in such networks aggregation occurs, leading to non-Newtonian blood behaviors especially in the presence of stenoses.

*Corresponding author

Email addresses: arthur.ghigo@dalembert.upmc.fr (A. R. Ghigo), pierre-yves.lagree@upmc.fr (P. -Y. Lagrée), fullana@lmm.jussieu.fr (J. -M. Fullana)

This 1D generalized non-Newtonian blood flow model will be useful in the future to improve our understanding of the global blood hemodynamics in micro and macro-circulation networks.

Keywords: arterial network, 1D model

---

1. Introduction

One-dimensional (1D) blood flow models are used in medical applications to provide physiological insights on hemodynamics in large networks of the macro- and micro-circulations. They capture the pulse wave propagation dynamics in large networks and enable for example patient-specific surgical planning [1, 2, 3]. The success of one-dimensional modelling relies on the speed and accuracy at which 1D models compute blood pressure, flow rate and cross-sectional area in elastic arteries and arterioles. In comparison, three-dimensional approaches are much more costly and time-consuming, especially in deformable elastic vessels and are therefore restricted to small networks of only a few arteries [4, 5, 6, 7]. Reduced-order models such as 1D models are also used to provide physiological boundary conditions to 3D approaches [8, 9, 4, 10].

In many regions of the systemic network, low shear regimes are reached (typically the shear rate $\dot{\gamma} \leq 1\ \mathrm{s}^{-1}$) as a consequence of the pulsatility of blood flow, of recirculation areas created by stenoses, aneurysms and bifurcations and of the decrease in shear with vessel ramification. In low shear regions, blood behaves as a non-Newtonian fluid and exhibits shear-thinning, viscoelastic and thixotropic behaviors. At low shear rates, molecular mechanisms trigger the aggregation of red blood cells (RBCs) into long column-like structures called "rouleaux", whereas at higher shear rates, these structures are deformed, disaggregated and the RBCs re-align in the direction of the flow. This reversible aggregation-disaggregation process is responsible for the shear-thinning behavior of blood. The different timescales of the aggregation and disaggregation processes are at the origin of the thixotropic response of blood. Finally, viscoelasticity stems from the elasticity of RBCs and the change of dissipation mechanisms at low

and high shear rates [11, 12, 13, 14, 15].

There exists strong evidence that the non-Newtonian behavior of blood influences the evolving of several cardiovascular pathologies, such as atherosclerosis, through local modifications of the hemodynamics [16]. Developing constitutive models of blood rheology is therefore of critical importance in cardiovascular simulations.

Existing non-Newtonian constitutive models can be roughly categorized as either time-independent or time-dependent models. Time-independent constitutive models describe only for the shear-thinning behavior of blood and are particularly relevant in shear-dominated steady flows [17, 18, 19]. Due to their simplicity, they are the most commonly used non-Newtonian blood flow models in two-dimensional (2D) and three-dimensional (3D) numerical simulations. Time-independent models have been applied to study intracranial aneurysms [20, 21], stenoses [22, 23], coronary arteries [24], idealized arterial trees [25, 26, 27, 28] and heart valves [29]. In most of these works, non-Newtonian effects were observed proving the relevance of modeling the complex rheology of blood. Time-dependent constitutive models include viscoelastic and thixotropic effects as well as shear-thinning effects in the steady flow limit. They were developed based on an analogy between blood and a viscoelastic Maxwell material [30]. In [31, 32], a generalized Maxwell model was derived based on polymer network theory, and successive improvements enabled the description of the Fahreus and Fahreus-Lindquist effects. In [33, 34, 35], a generalized Oldroyd-B model was proposed and improved based on a thermodynamics approach. Time-dependent models were successfully incorporated into 3D simulations [36, 37, 38, 39, 35] and good agreement was found with experimental data in simple steady and pulsatile flows.

However, in almost every application previously mentioned, the mechanics and distensibility of the vessel wall were neglected. Moreover, non-Newtonian effects in large networks of arteries have seldom been studied. Even in 1D applications blood is almost always assumed Newtonian. Only in [40, 41] the authors considered the non-Newtonian behavior of blood, respectively using a model

proposed in [42] and a power-law model. In [43], the authors have proposed a reduced-order non-Newtonian model with a particular focus on the thixotropic behaviors of the yield stress. However, the authors obtained a semiquantitative agreement with experimental data from Bureau [44, 14] and Sousa [45] and the model was not coupled to a blood flow numerical solver.

The goal of this work is to provide a simple and accurate 1D time-dependent non-Newtonian blood flow model and apply it to study large networks of elastic arteries. The rheological model we propose involves a simplified viscoelastic Maxwell model with shear and structure dependent coefficients and a kinetic equation describing the aggregation-disaggregation of RBCs which are considered as a homogeneous single phase.

In Section 2 we present the 1D blood flow model, the non-Newtonian shear stress model and its integration in the 1D blood flow model. In section 3, we describe analytic solutions of the rheological model in different flow conditions exhibiting shear-thinning, thixotropic and viscoelastic behaviors. Then, in section 4 we compare the results of the model to published experimental rheological data. Finally, in sections 5 and 6 we investigate the influence of the non-Newtonian model on blood flow in synthetic arterial networks with and without stenoses.

2. One-dimensional time-dependent non-Newtonian blood flow model

2.1. Derivation of the one-dimensional blood flow model

Assuming that blood is an incompressible fluid, blood flow is governed by the 3D incompressible Navier-Stokes equations:

$$\begin{cases} \boldsymbol{\nabla} \cdot \boldsymbol{u} = 0 & \text{(1a)} \\ \rho \left[\partial_t \boldsymbol{u} + \boldsymbol{u} \cdot \boldsymbol{\nabla} \boldsymbol{u}\right] + \boldsymbol{\nabla} \cdot \left[p\mathbb{I} - \boldsymbol{\tau}\right] = 0, & \text{(1b)} \end{cases}$$

where ρ is the density, supposed constant, p is the pressure, $\boldsymbol{u}$ is the velocity vector, $\mathbb{I}$ is the identity tensor and $\boldsymbol{\tau}$ is the stress tensor.

Two main hypotheses are involved in the derivation of the 1D blood flow model. First, the flow is assumed to be axisymmetric, implying that the geometry and both the inlet and outlet boundary are also axisymmetric. Second, the radius R of the artery is considered small with respect to the wavelength λ of the cardiac pulse wave, which is the characteristic axial lengthscale. In physiological conditions, $R = 1$ cm and $\lambda_{pulse} = 100$ cm, and we refer to this assumption as the long-wave hypothesis. Combining both hypotheses we obtain the reduced Navier-Stokes-Prandtl (RNS-P) equations [46], describing the conservation of mass and the balance of axial momentum:

$$\begin{cases} \dfrac{1}{r}\dfrac{\partial}{\partial r}\left[r u_r\right] + \dfrac{\partial u_x}{\partial x} = 0 & \text{(2a)} \\ \dfrac{\partial u_x}{\partial t} + u_r\dfrac{\partial u_x}{\partial r} + u_x\dfrac{\partial u_x}{\partial x} = -\dfrac{1}{\rho}\dfrac{\partial p}{\partial x} + \dfrac{1}{\rho r}\dfrac{\partial}{\partial r}\left(r\tau_{rx}\right) & \text{(2b)} \\ p = p\left(x,t\right). & \text{(2c)} \end{cases}$$

It is important to note that due to the long-wave hypothesis, the pressure p depends only on the axial position x and the only non zero shear stress component of $\boldsymbol{\tau}$ is τ_{rx}.

We then integrate the RNS-P equations (2a) and (2b) over the cross-sectional area of an artery of length L (see Figure 1) . Through this exact integration or averaging process, we obtain the 1D mass and momentum equations expressed at time t in the axial position x:

$$\begin{cases} \dfrac{\partial A}{\partial t} + \dfrac{\partial Q}{\partial x} = 0 & \text{(3a)} \\ \dfrac{\partial Q}{\partial t} + \dfrac{\partial}{\partial x}\left[\psi\dfrac{Q^2}{A}\right] + \dfrac{A}{\rho}\dfrac{\partial p}{\partial x} = \dfrac{2\pi R}{\rho}\tau_{rx}|_{r=R}. & \text{(3b)} \end{cases}$$

The variables A and Q are respectively the averaged cross-sectional area and the axial flow rate defined as:

$$A = 2\pi\int_{r=0}^{R} r\mathrm{d}r, \quad Q = 2\pi\int_{r=0}^{R} u_x r\mathrm{d}r, \tag{4}$$

where R is the instantaneous radius of the artery. Finally, the shape factor ψ is defined as:

$$\psi = 2\pi\frac{A}{Q^2}\int_{r=0}^{R} r u_x^2\mathrm{d}r, \tag{5}$$

and depends on the axial velocity profile lost in the averaging process. We therefore assume an *a priori* shape of the velocity profile and set $\psi = 1$ corresponding to a flat velocity profile assumption.

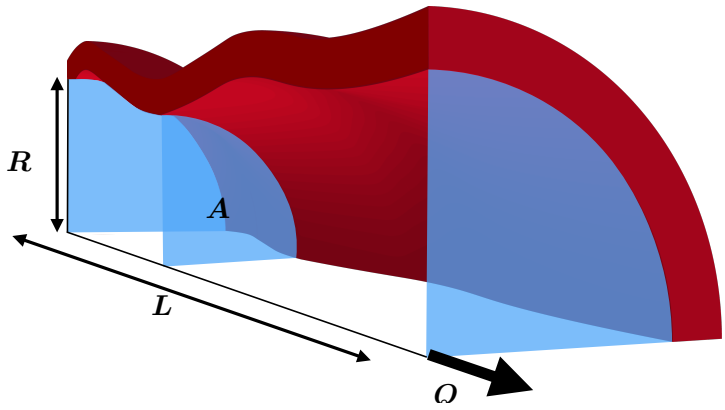

Figure 1: One-dimensional representation of the fluid domain contained in an axisymmetric cylindrical artery. For clarity, only one-fourth of the artery of length L is represented. The variable Q is the flow rate and $A = \pi R^2$ is the cross-sectional area of the artery.

The closure relation connecting the cross-sectional area A and the pressure p is provided by thin-cylinder theory:

$$p = p_{ext} + K\left[\sqrt{A} - \sqrt{A_0}\right] + \nu_v \frac{\partial A}{\partial t}, \tag{6}$$

where p_{ext} is the external pressure and A_0 is the neutral cross-sectional area. The viscoelastic behavior of the arterial wall is described by a Kelvin-Voigt model where the coefficients K and ν_v model respectively the arterial rigidity and the viscoelasticity of the wall. More details on the viscoelastic behavior of the arterial wall can be found in [47].

The last remaining unknown is the wall shear stress (WSS) $\tau_{rx}|_{r=R}$ and the derivation for Newtonian and non Newtonian fluids will be the subject of the following subsections 2.2 and 2.3.

2.2. Stress model: Newtonian

We briefly discuss here the derivation of the WSS $\tau_{rx}|_{r=R}$ in the case of a Newtonian fluid in the 1D framework. Under Newtonian hypothesis, the shear stress τ_{rx} can be expressed as a function of a constant viscosity μ and the shear rate:

$$\tau_{rx} = \mu \left[\frac{\partial u_r}{\partial x} + \frac{\partial u_x}{\partial r} \right]. \tag{7}$$

The long-wave approximation allows us to simplify the expression for the shear rate at the wall $\dot{\gamma}|_{r=R}$:

$$\dot{\gamma}|_{r=R} \approx \frac{\partial u_x}{\partial r}|_{r=R}, \tag{8}$$

and we obtain the following Newtonian WSS model:

$$\tau_{rx}|_{r=R} = \mu \dot{\gamma}|_{r=R}. \tag{9}$$

Furthermore, the 1D closure hypotheses suggest that we may rewrite the axial velocity u_x as:

$$u_x\left(x, r, t\right) = \phi\left(\frac{r}{R\left(x,t\right)}, t\right) U\left(x,t\right), \tag{10}$$

where $U = Q/A$ is the averaged velocity and ϕ is the shape of the velocity profile. The expression for the wall shear rate then becomes:

$$\dot{\gamma}|_{r=R} = U \frac{\partial \phi}{\partial r}|_{r=R}. \tag{11}$$

The average velocity U can be computed using the 1D model (equations (3)). However, as was mentioned before in 2.1 the shape of the velocity profile ϕ is lost in the integration process and remains an unknown of the problem. We must therefore once again assume an *a priori* shape of the velocity profile. For example, for a Couette flow $\dot{\gamma} = -U/R$, for a Poiseuille flow $\dot{\gamma} = -4U/R$ and it is common in large arteries to use $\dot{\gamma} = -11U/R$ [48, 49]. Without loss of generality, we assume in the following that $\dot{\gamma} = -U/R$.

Combining the previous equations, we finally obtain a closed-form expression for the Newtonian WSS:

$$\tau_{rx}|_{r=R} = -\mu \frac{U}{R}, \tag{12}$$

and we recover the classical viscous contribution $C_f U$ in the 1D momentum equation (3b), with $C_f = -2\pi\nu$. For clarity reasons, we drop the subscript $|_{r=R}$ in the following and write the WSS as τ_{rx} and the shear rate as $\dot{\gamma}$.

2.3. Stress model: non-Newtonian

Following the approach proposed in [31], we build a transient reduced-order constitutive model for blood. We first split the WSS into a structural and a Newtonian component:

$$\tau_{rx} = \tau_{st} + \mu_\infty \dot{\gamma}, \tag{13}$$

where τ_{st} represents the structure dependent stress and μ_∞ the viscosity of blood in the high-shear asymptotic limit. We describe the time and space evolution of τ_{st} using the generalized Maxwell equations involving the Jaumann derivative of τ_{st}. Using the 1D long-wave and axisymmetric hypotheses, these equations simplify into a 1D viscoelastic Maxwell equation, representing the combined contributions of an elastic spring and a viscous dashpot:

$$\lambda_{st} \frac{\partial \tau_{st}}{\partial t} + \tau_{st} = 2\mu_{st}\dot{\gamma} \tag{14}$$

where λ_{st} is a characteristic elastic relaxation time and μ_{st} is the structural viscosity.

Next, we introduce a structure dependence in the Maxwell equation (14). We assume that the whole structure of blood, comprising of RBCs and rouleaux, can be described by a single parameter f varying between 0 for a completely disaggregated structure and 1 for a fully aggregated one. We then hypothesize that both λ_{st} and μ_{st} linearly depend on this structure parameter f:

$$\begin{cases} \lambda_{st} = \lambda_a f & \text{(15a)} \\ \mu_{st} = [\mu_0 - \mu_\infty]\, f. & \text{(15b)} \end{cases}$$

where λ_a is a characteristic aggregation time and μ_0 is the viscosity of blood in the low shear asymptotic limit. The equations (15a) and (15b) express the simplest possible dependence between the structure parameter f and the blood parameters.

Using an approach inspired from polymer theory [11, 31], we describe the evolution of f using kinetic equation representing the transport of f and the competition between aggregation and disaggregation of blood structure:

$$\frac{\partial f}{\partial t} + U\frac{\partial f}{\partial x} = \frac{1-f}{\lambda_a} - \frac{f}{\lambda_d}, \tag{16}$$

where λ_d is a characteristic disaggregation time. As shear is the driving disaggregation mechanism, we define λ_d as the inverse of the shear rate $\dot{\gamma}$:

$$\lambda_d = \frac{1}{\delta|\dot{\gamma}|}, \tag{17}$$

where δ is a fitting coefficient. Compared to other existing simplified structural models, we incorporate advection in the kinetic equation as structure parameter f is transported by the blood flow in the arteries.

Finally, yield stress could be taken into account through the change of variables $\tau_{st}^{'} = \tau_{st} - \tau_y$, where τ_y is the yield stress. However, we assume that $\tau_y = 0$ in the following. We also neglect the effects of hematocrit variations and suppose a fixed hematocrit $H = 0.45$ (45% of blood volume occupied by RBCs). Nevertheless, these effects could be included in the model through a transport equation for H and hematocrit dependent coefficients (see [42] for details).

2.4. Time-dependent 1D non-Newtonian blood flow model

Replacing the pressure p by its expression (6), we obtain the closed-form 1D system of equations, describing the conservation of mass and the balance of momentum in a viscoelastic artery:

$$\begin{cases} \dfrac{\partial A}{\partial t} + \dfrac{\partial Q}{\partial x} = 0 & \text{(18a)} \\ \dfrac{\partial Q}{\partial t} + \dfrac{\partial}{\partial x}\left[\dfrac{Q^2}{A} + \dfrac{K}{3\rho}A^{\frac{3}{2}}\right] = \dfrac{2\pi R}{\rho}\tau_{rx} + C_\nu \dfrac{\partial^2 Q}{\partial x^2}. & \text{(18b)} \end{cases}$$

with:

$$\begin{cases} \dot{\gamma} = -\dfrac{U}{R} & \text{(19a)} \\ \tau_{rx} = \tau_{st} + \mu_\infty \dot{\gamma} & \text{(19b)} \\ \lambda_{st} \dfrac{\partial \tau_{st}}{\partial t} + \tau_{st} = 2\mu_{st}\dot{\gamma} & \text{(19c)} \\ \dfrac{\partial f}{\partial t} + U \dfrac{\partial f}{\partial x} = \dfrac{1-f}{\lambda_a} - \dfrac{f}{\lambda_d} & \text{(19d)} \\ \mu_{st} = [\mu_0 - \mu_\infty]\, f & \text{(19e)} \\ \lambda_{st} = \lambda_a f & \text{(19f)} \\ \lambda_d = \dfrac{1}{\delta|\dot{\gamma}|}, & \text{(19g)} \end{cases}$$

where μ_0, μ_∞, λ_a and δ are constants to be determined using available rheological data.

2.5. Numerical scheme

From a mathematical point of view the system (equations (18)) is hyperbolic. In physiological conditions, the flow speed is smaller than the wave speed, therefore the flow is always subcritical and shock-like phenomena do not occur. To capture the propagation of pulse waves, we solve the system (18) using a second-order Adam-Bashforth time-integration scheme coupled to a *finite-volume* kinetic numerical scheme [2, 50]. The rheological system (equations (19)) is explicitly updated using the same time integration scheme as the hyperbolic system (18) and the transport equation is solved using a classical upwind scheme, where the velocity is given by the kinetic numerical flux [51].

The treatment of inlet and outlet boundary conditions as well as bifurcations is classical and we refer the readers to [52, 53, 50] for more details.

3. Analysis of the non-Newtonian stress model

We analyze the time-dependent behavior of the 1D non-Newtonian stress model (equations (19)) derived in the previous section. To simplify the analysis,

we consider idealized flow conditions where we assume that all quantities are independent of the axial position x, and hence decouple the rheological model (19) from the 1D blood flow model (18).

3.1. Steady flow: Analogy with the simplified Cross model

We consider a steady flow, for which the rheological model (19) simplifies to:

$$\begin{cases} f_s = \dfrac{1}{1+\frac{\lambda_a}{\lambda_d}} & \text{(20a)} \\ \tau_s = \mu_{st}\dot{\gamma} = \left[\mu_0 - \mu_\infty\right] f_s \dot{\gamma} & \text{(20b)} \end{cases}$$

This steady state is then a consequence of the balance between aggregation and disaggregation, and the equilibrium value of the structure function (20a) explicitly depends on the aggregation time scales λ_a and λ_d where

- if $\lambda_a \gg \lambda_d$, we have $f \approx 0$ and structure disaggregation process is dominant;
- if $\lambda_a \ll \lambda_d$, at the contrary $f \approx 1$ and structure aggregation process is dominant.

In this steady case, we can explicitly define the apparent viscosity $\mu\left(\dot{\gamma}\right) = \frac{\tau_{rx}}{\dot{\gamma}}$ using equations (20a) and (20b) which gives

$$\mu\left(\dot{\gamma}\right) = \mu_{st} + \mu_\infty = \mu_\infty + \frac{\mu_0 - \mu_\infty}{1+\frac{\lambda_a}{\lambda_d}}, \tag{21}$$

exhibiting the expected shear-thinning behavior. Equation (21) is identical to the simplified Cross constitutive model [54]:

$$\mu = \mu_\infty + \frac{\mu_0 - \mu_\infty}{1+\lambda_c\dot{\gamma}}. \tag{22}$$

By analogy with (21) we have:

$$\lambda_c = \lambda_a \delta. \tag{23}$$

Table 1 summarizes the parameter values of the simplified Cross constitutive model taken from [17]. In the following, we use the values of μ_0 and μ_∞ pre-

μ_∞ [poise]	μ_0 [poise]	λ_c [s]
0.05	1.3	8

Table 1: Parameter values of the simplified Cross constitutive model taken for [17]

sented in Table 1. We determine the remaining unknown parameters λ_a and δ using the value of the constant λ_c and experimental data presented in [15]. The complete set of parameters of the rheological model (19) is presented in Table 2.

3.2. Constant shear rate $\dot{\gamma}$

We study now the disaggregation under a constant shear rate $\dot{\gamma}_c$ of a fluid initially at rest. At $t = 0$, we assume that $f = 1$ and $\tau_{st} = 0$. The kinetic equation for the structure function is:

$$\frac{\mathrm{d}f}{\mathrm{d}t} = \frac{1-f}{\lambda_a} - \frac{f}{\lambda_d}. \tag{24}$$

The solution is:

$$f = f_\infty + [1 - f_\infty]\, \mathrm{e}^{-\frac{t}{\lambda_c}}, \tag{25}$$

where $f_\infty = \frac{\lambda_c}{\lambda_a}$ and $\frac{1}{\lambda_c} = \frac{1}{\lambda_a} + \frac{1}{\lambda_d}$. Injecting the expression (25) in equation (14) we obtain the following expression for the structure stress τ_{st}:

$$\tau_{st} = [\mu_0 - \mu_\infty]\, \dot{\gamma}_c \frac{[1 - f_\infty]\, \frac{t}{\lambda_a} + [f_\infty]^2 \left[\mathrm{e}^{\frac{t}{\lambda_c}} - 1\right]}{1 + f_\infty \left[\mathrm{e}^{\frac{t}{\lambda_c}} - 1\right]}. \tag{26}$$

When $t \to \infty$, we find the asymptotic values of f and τ_{st}:

$$\begin{cases} f_{t\to\infty} = f_\infty & \text{(27a)} \\ \tau_{st,t\to\infty} = [\mu_0 - \mu_\infty]\, \dot{\gamma}_c f_\infty. & \text{(27b)} \end{cases}$$

System (27) is identical to the steady system (20). The model therefore exhibits a characteristic viscoelastic property, that is the transitions from an initially aggregated state ($f = 1$, $\tau_{st} = 0$) towards a steady equilibrium state (equations (27)) where aggregation and disaggregation are perfectly balanced.

At intermediate times $0 < t < \infty$, the model exhibits a thixotropic behavior depending on the choice of the characteristic aggregation and disaggregation timescales λ_a and λ_d. Indeed, for given values of λ_a and λ_d, it is possible to find the analytic expression for the time $t_{\tau,max}$ at which the maximum value of τ_{st} is reached:

$$t_{\tau_{st,max}} = \lambda_c \left[1 + \frac{1}{1 - \frac{\lambda_c}{\lambda_a}} + W\left(\left[\frac{\lambda_a}{\lambda_c} - 1 \right] \mathrm{e}^{-\left[1 + \frac{1}{1 - \frac{\lambda_c}{\lambda_a}} \right]} \right) \right], \tag{28}$$

with:

$$\tau_{st,max} = \tau_{st,t\to\infty} \left[1 + W\left(\left[\frac{\lambda_a}{\lambda_c} - 1 \right] \mathrm{e}^{-\left[1 + \frac{1}{1 - \frac{\lambda_c}{\lambda_a}} \right]} \right) \right], \tag{29}$$

where W is the *Lambert-W* function, which is the inverse function of $f(w) = we^w$. From the above expressions (28) and (29), simple calculations allow us to show that $0 < t_{\tau_{st,max}} < \infty$ and $\tau_{st,max} \geq \tau_{st,t\to\infty}$. We can therefore conclude that in this configuration the model exhibits a characteristic thixotropic behavior at finite time, represented by an overshoot of the structure shear stress τ_{st} with respect to the asymptotic steady value $\tau_{st,t\to\infty}$. The magnitude of the overshoot depends on the value of the characteristic aggregation times λ_a and λ_d where two

- if $\lambda_a \gg \lambda_d$ (equivalently $\dot{\gamma} \gg 1\ \mathrm{s}^{-1}$), than $\lambda_c \approx \lambda_d$ and we have:

$$\tau_{st,max} \gg \tau_{st,t\to\infty}. \tag{30}$$

  Disaggregation occurs at a much smaller timescale than aggregation due to the high shear rate value. This results in large variations of the structure of blood at small times ($t \leq t_d$) and therefore a large overshoot of the structure shear stress τ_{st} before the system relaxes towards the steady state.

- if $\lambda_a \ll \lambda_d$ (equivalently $\dot{\gamma} \ll 1\ \mathrm{s}^{-1}$), than $\lambda_c \approx \lambda_a$ and we have:

$$\tau_{st,max} \approx \tau_{st,t\to\infty}. \tag{31}$$

Aggregation occurs at a much smaller timescale than disaggregation due to the low shear rate value. The consequence is almost no variation of the structure of blood and therefore no overshoot of the structure shear stress τ_{st}.

3.3. Zero shear rate $\dot{\gamma}$

We study here the reaggregation of a fluid at rest. At $t = 0$, we assume that $f = f_0$ and $\tau_{st} = \tau_{st,0}$. The kinetic equation for the structure function is:

$$\frac{\mathrm{d}f}{\mathrm{d}t} = -\frac{1+f}{\lambda_a}. \tag{32}$$

The solution is straightforward:

$$f = 1 + [f_0 - 1]\,\mathrm{e}^{-\frac{t}{\lambda_a}}. \tag{33}$$

Injecting expression (33) in equation (14) we obtain the following expression for the structure stress τ_{st}:

$$\tau_{st} = \tau_{st,0}\frac{f_0}{f_0 - 1 + \mathrm{e}^{\frac{t}{t_a}}}. \tag{34}$$

When $t \to \infty$, we find as before the asymptotic values of f and τ_{st} :

$$\begin{cases} f_{t\to\infty} = 1 & \text{(35a)} \\ \tau_{st,t\to\infty} = 0. & \text{(35b)} \end{cases}$$

The model exhibits here another characteristic viscoelastic property, that is the relaxation towards a fully aggregated state. The phenomenon is driven only by the characteristic aggregation timescale λ_a as in the absence of shear $\lambda_d \to \infty$.

The asymptotic analysis conducted in this section highlights the shear-thinning, viscoelastic and thixotropic behaviors of the rheological model (equations (19)) proposed in the previous section. In the following sections, we compare the numerical results, where spatial variations occur, to the analytic results previously obtained and to experimental results in order to assess if the model is able to quantitatively describe the flow behavior of blood.

4. Comparison with experimental data

We propose to compare the numerical results of the 1D non-Newtonian model (18)–(19) to experimental data available in the literature. We use published results of Bureau et al. [14] and McMillan [55], where the authors systematically studied the response of blood to step and triangular shear solicitations using a coaxial cylinder microviscometer.

In subsections 4.1, 4.2 and 4.3, we consider a single artery where we impose the flow rate at the inlet and a non-reflecting boundary condition at the outlet. The time-evolution of the inlet flow rate depends on the considered experimental test case. Its magnitude is given by the following expression, designed to impose a chosen shear rate $\dot{\gamma}_{in}$:

$$Q_{in}\left(\dot{\gamma}_{in}\right) = \frac{1}{\frac{\partial \phi}{\partial r}} A \dot{\gamma}_{in} \tag{36}$$

We recall that without loss of generality, we use $\frac{\partial \phi}{\partial r}|_{r=R} = -\frac{1}{R}$. We assume that blood enters the artery in a fully disaggregated state ($f = 0$). For each simulation, the initial conditions are the asymptotic behavior of a fluid at rest:

$$\begin{cases} Q = 0 \quad \text{and} \quad A = A_0 & \text{(37a)} \\ f = 1 \quad \text{and} \quad \tau_{st} = 0. & \text{(37b)} \end{cases}$$

The parameters of the blood constitutive model (19) are summarized in Table 2. The geometrical and mechanical parameters describing the artery are given in Table 3. Finally, the time- and space-discretization parameters are described in Table 4.

ρ [g $\cdot$ cm^{-3}]	μ_∞ [poise]	μ_0 [poise]	λ_a [s]	δ
1	0.05	1.3	5	1.5

Table 2: Parameters of the blood constitutive model (19), given in *cgs* units and based on an analogy with the simplified Cross constitutive model [54] and experimental data from [15].

L [cm]	A [cm^2]	K [dyne $\cdot$ cm^{-3}]	C_v [cm$^2 \cdot$ s^{-1}]
10	1	10^4	0

Table 3: Geometrical and mechanical parameters describing the artery, given in *cgs* units.

Δt [s]	Δx [cm]	Order
10^{-4}	5 10^{-2}	2

Table 4: Numerical parameters describing the time discretization and the mesh.

4.1. Single shear-step

In a series of experiments, Bureau *et al.* [44] obtained experimental data on the behavior of a blood sample subjected to a step-change in shear rate:

$$\dot{\gamma}(t) = \begin{cases} \dot{\gamma}_{1,2} & \text{for} \quad 0 \leq t < \Delta t_{1,2} \\ 0 & \text{for} \quad \Delta t_{1,2} \leq t. \end{cases} \tag{38}$$

To highlight separately the viscoelastic and thixotropic behaviors of blood, they considered a low shear regime for which ($\dot{\gamma}_1 = 0.05$ s^{-1} and $\Delta t_1 = 30$ s) and a high shear regime ($\dot{\gamma}_2 = 1$ s^{-1} and $\Delta t_2 = 8.5$ s).

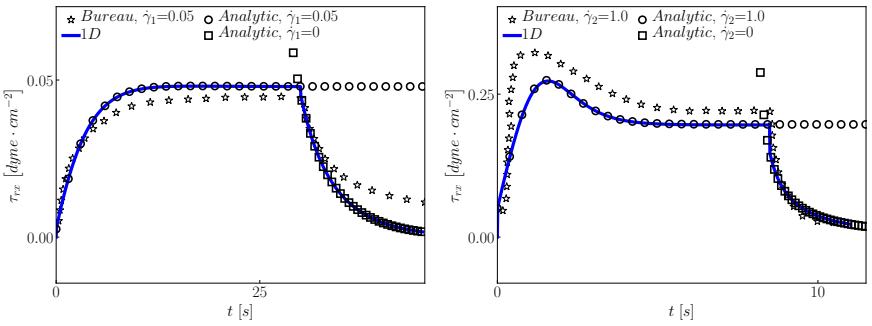

Figure 2: Time evolution of the shear stress τ_{rx} with a step-change in shear rate: comparison between experimental data from Bureau [44] (☆), results of the 1D blood flow model (18) (—) and analytic solutions (26) (○) and (34) (□). Left: Low shear viscoelastic regime with $\dot{\gamma}_1 = 0.05$ s^{-1} for $\Delta t_1 = 30$ s and then $\dot{\gamma}_1 = 0$ s^{-1}. Right: High shear thixotropic regime (overshoot) with $\dot{\gamma}_2 = 1$ s^{-1} for $\Delta t_2 = 8.5$ s and then $\dot{\gamma}_2 = 0$ s^{-1}. There is a qualitative and quantitative match between experimental data and numerical results, and a perfect match between analytic and numerical results.

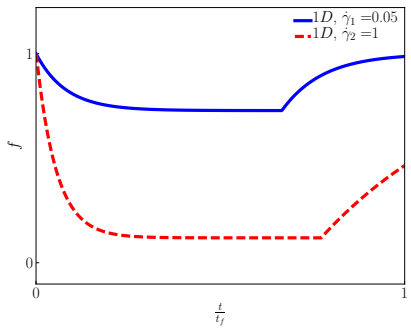

Figure 3: Time evolution of the structure function f with a step-change in shear rate, computed using the 1D blood flow model (18): low shear viscoelastic regime with $\dot{\gamma}_1 = 0.05$ s^{-1} for $\Delta t_1 = 30$ s (—), high shear thixotropic regime with $\dot{\gamma}_2 = 1$ s^{-1} for $\Delta t_2 = 8.5$ s (– –). In the high shear regime, there is a large decrease of the structure function on a short timescale, leading to the thixotropic behavior observed in Figure 2 right.

In Figure 2, we compare the measured experimental shear stress to the 1D numerical shear stress computed by mimicking the experimental flow conditions. As these flow conditions are similar to those studied analytically in subsections 3.2 and 3.3, we also compare the experimental and numerical shear stresses to the analytic solutions (equations (26) and (34)). We observe that for both flow conditions $\dot{\gamma}_1$ and $\dot{\gamma}_2$, the experimental data from Bureau [44] agree qualitatively and semiquantitatively with the 1D numerical results. Moreover, the analytic and 1D numerical results are perfectly matched. The data presented in Figure 2 Left are characteristic of a viscoelastic material: the shear stress rises continuously towards the equilibrium steady value, and then relaxes in the absence of shear towards a fully aggregated state. On the contrary, the data plotted in Figure 2 Right present the characteristic overshoot of a thixotropic material. Both rheological behaviors of blood were analyzed in subsection 3.2 and can be explained focusing on the evolution of the structure parameter f, presented in Figure 3. At low shear values ($\dot{\gamma}_1$), the structure of blood is not significantly altered. At higher shear rates ($\dot{\gamma}_2$), large variations of the structure of blood occur on a short timescale, leading to memory effects and a thixotropic overshoot of the shear stress.

The comparison with analytic solutions validates the 1D numerical scheme and the agreement with experimental results indicates that systems (18)-(19) using the set of parameters presented in Table 2 provide a satisfactory description of the time-dependent behavior of blood.

4.2. Multiple shear-steps

Experimental data from McMillan *et al.* [55] describe the time-dependent shear stress response of blood to two successive tome shear-steps of amplitude $\dot{\gamma} = 8$ s^{-1} and of length $\Delta t = 2.5$ s. The experiment was repeated three times, each time decreasing the time delay Δt_d between the consecutive shear-steps, during which no shear was applied.

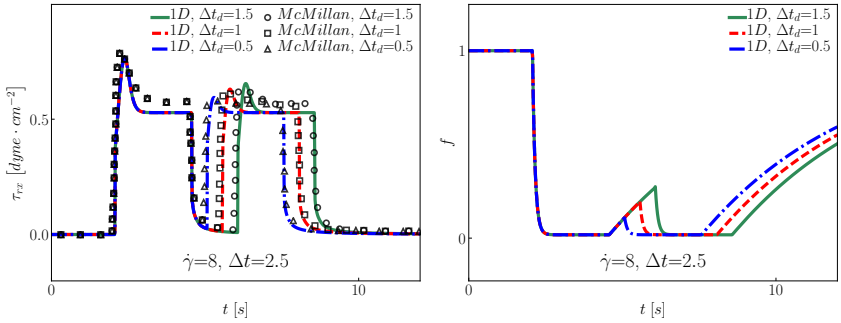

Figure 4: Time evolution of the shear stress τ_{rx} (left) and the structure function f (right) with two successive step-changes in shear rate of amplitude $\dot{\gamma} = 8$ s^{-1} and of length $\Delta t = 2.5$ s: comparison between experimental data from McMillan [55] and numerical results of the 1D blood flow model (18) for a time delay $\Delta t_d \in \{1.5$ (exp. ○, 1D —$)$, 1 (exp. □, 1D – –$)$, 0.5 (exp. △, 1D – -$)\}$ s. There is a qualitative and quantitative agreement between experimental and numerical data. The thixotropic overshoot increases with Δt_d as structure variations are more important.

In Figure 4 Left, we compare the time evolution of the experimental and 1D numerical shear stresses for different time delays $\Delta t_d \in \{1.5, 1, 0.5\}$. Both solutions are qualitatively and quantitatively comparable and we observe the expected viscoelastic relaxation and thixotropic transient overshoot. Results in Figure 4 Right correlate the increase of the overshoot amplitude with larger

variations of the structure parameters f, as blood has more time to reaggregate when Δt_d increases.

4.3. Triangle shear solicitation

Bureau *et al.* [14] also obtained experimental hysteresis curves by imposing a triangular shear rate solicitation to the blood sample:

$$\dot{\gamma}(t) = \begin{cases} \dot{\gamma}_{1,2} \dfrac{t}{t_{1,2}} & \text{for} \quad 0 \leq t < t_{1,2} \\ \dot{\gamma}_{1,2} \left[2 - \dfrac{t}{t_{1,2}} \right] & \text{for} \quad t_{1,2} \leq t \leq 2t_{1,2}. \end{cases} \tag{39}$$

To still highlight the viscoelastic and thixotropic behaviors of blood, the authors considered a low shear regime ($\dot{\gamma}_1 = 0.12$ s^{-1} and $t_1 = 13$ s) and a high shear regime ($\dot{\gamma}_2 = 1.03$ s^{-1} and $t_2 = 47.6$ s).

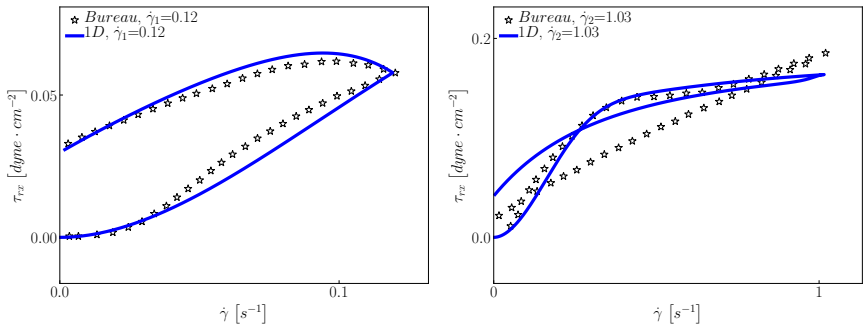

Figure 5: Hysteresis curves of the evolution the shear stress τ_{rx} as a function of the shear rate $\dot{\gamma}$ under a triangular shear solicitation: comparison between experimental data from Bureau [14] (☆) and 1D numerical results (—). Left: Low shear viscoelastic regime with $\dot{\gamma}_1 = 0.12$ s^{-1} and $t_1 = 13$ s. Right: High shear thixotropic regime with $\dot{\gamma}_2 = 1.03$ s^{-1} and $t_2 = 47.6$ s. There is a qualitative and quantitative match between experimental data and numerical results.

In Figure 5, we plot the experimental and numerical variations of the shear stress τ_{rx} with respect to the shear rate $\dot{\gamma}$. In the low-shear regime $\dot{\gamma}_1$ plotted in Figure 5 Left, the viscoelastic behavior of blood is highlighted and the experimental and numerical results match very well. In the high-shear regime displayed on Figure 5 Right, thixotropic effect are dominant. For the increasing shear region of the curve, the experimental and numerical results are well

matched. However, for the decreasing shear part, the experimental behavior is not reproduced, even though the shear stress amplitudes are similar.

The results presented in subsections 4.1, 4.2 and 4.3 indicate that the 1D blood flow model (18) coupled to the rheological model (19) allows us to compute numerical results similar to well-known experimental data form [44, 44, 55]. We can now move towards more complex simulation in large networks of elastic arteries.

5. Elementary bifurcation

Bifurcations are elementary parts of an arterial network and connect a parent artery p to two daughter arteries d_1 and d_2. Bifurcations are responsible for the reflection of the incoming pulse wave as they represent impedance discontinuities in the network, and due to the complex flow patterns they generate the non-Newtonian behavior of blood can be particularly important in these configurations.

In a symmetric bifurcation, we compare here the 1D non-Newtonian blood flow model (18)–(19) with its Newtonian counterpart. The geometrical and mechanical properties of the bifurcation are presented in Table 5 and correspond to average properties of large arteries. At the inlet of the parent artery p, we impose the flow rate Q_{in} to mimic the behavior of the heart:

$$Q_{in}(t) = Q_h \max\left(0, \sin\left(2\pi \frac{t}{T_h}\right)\right), \quad 0 \leq t \leq 10T_h, \tag{40}$$

with $T_h = 1$ s. We choose the maximum flow rate $Q_h \in \{1, 10, 100\}$ cm$^3 \cdot$s^{-1} to describe the flow in different regions of the systemic network. We also assume that blood enters the artery in a fully disaggregated state ($f = 0$). At the outlet of the daughter arteries d_1 and d_2, we set a non-reflecting boundary condition as in section 4. Finally, the initial conditions are (37) and the time- and space-discretization parameters of the network are described in Table 4. We present data obtained after 4 periods to ensure that the system has reached a periodic state.

L_{p,d_1,d_2} [cm]	R_{p,d_1,d_2} [cm]	K_{p,d_1,d_2} [dyne $\cdot$ cm^{-3}]	C_v [cm$^2 \cdot$ s^{-1}]
10	1	10^4	0

Table 5: Geometrical and mechanical parameters describing the properties of the parent artery p and the daughter arteries d_1 and d_2, given in *cgs* units.

In Figure 6, we compare the structure f (left), shear stress τ_{rx} (middle) and pressure p (right) waveforms computed with the Newtonian and non-Newtonian 1D blood flow model; numerical data are taken in the middle of the parent artery p and the daughter artery d_1. We do not present results for the artery d_2 as they are to artery d_1 due to the symmetry. As we decrease the flow rate ($Q = 100$ cm$^3 \cdot$s^{-1} to $Q = 1$ cm$^3 \cdot$s^{-1} from top to bottom in Figure 6), the shearing forces decrease allowing the RBCs to aggregate. As a consequence, in both arteries the structure function f and the shear stress $|\tau_{rx}|$ increase compared to the Newtonian case, with up to 100% differences for $Q_h = 1$ cm$^3 \cdot$s^{-1}. The pressure then rises to compensate the increased viscous stresses and maintain the normal flow. Note that the value of f is higher and the value of $|\tau_{rx}|$ is lower in artery d_1 than in artery p as the flow coming from artery p splits in two to vascularize both daughter arteries.

These results indicate that non-Newtonian effects are important in certain bifurcations and can lead to modification of the WSS stress patterns and an increase of pressure. They are corroborated by similar data obtained in different 3D studies [27, 24] of bifurcations. In the following, we extend this analysis to non-Newtonian effects in large networks of arteries.

6. Idealized asymmetric network

Reduced-order 1D blood flow models have been designed to capture the wave propagation dynamics in large networks. We want to analyze how non-Newtonian effects affect the network hemodynamics using the 1D time-dependent non-Newtonian model (equations (18)–(19)).

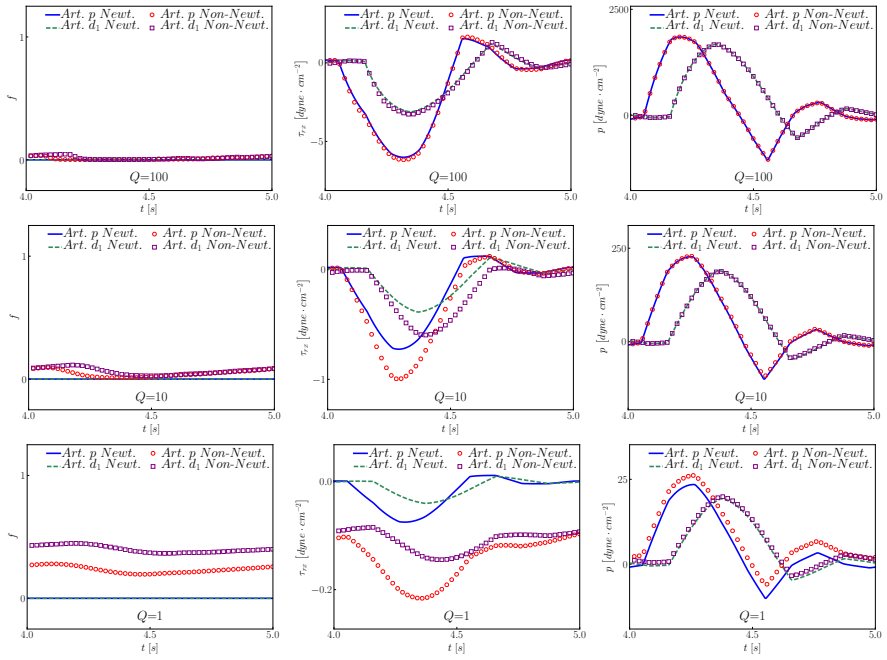

Figure 6: Temporal evolution of the structure function f (left), the shear stress τ_{rx} (middle) and the pressure p (right) taken in the middle of parent artery p and the daughter artery d_1. Top: $Q = 100$ cm$^3 \cdot$ s^{-1}. Center: $Q = 10$ cm$^3 \cdot$ s^{-1}. Bottom: $Q = 1$ cm$^3 \cdot$ s^{-1}. We compare the results of the Newtonian (artery p —, artery d_1 – –) and the non-Newtonian (artery p ○, artery d_1 □) 1D blood flow models. As the flow rate decreases, the aggregation increases, leading to a higher shear stress $|\tau_{rx}|$ and an increase of the pressure p.

We consider an idealized asymmetric arterial tree made only of elementary bifurcations linked together to form a network. In each elementary bifurcation a parent artery p connects to two daughter arteries d_α and d_β. Given the mechanical and geometrical properties of the parent artery p, we construct the daughter arteries using the relationships presented in [56, 57] and used more recently in [58, 40], which describe the physiological evolution the arteries' geometrical and

mechanical properties along the network:

$$\begin{cases} R_\alpha = \alpha R_p & \text{(41a)} \\ R_\beta = \beta R_p & \text{(41b)} \\ L = 50R & \text{(41c)} \\ K = \dfrac{4}{3}\dfrac{R}{\sqrt{pi}}\left[k_1 \mathrm{e}^{k_2 R} + k_3\right] & \text{(41d)} \\ \dot{\gamma} = -4\dfrac{U}{R}, & \text{(41e)} \end{cases}$$

where $\alpha = 0.9$ and $\beta = 0.6$ are asymmetry coefficients and $k_1 = 2 \times 10^7$ dyne $\cdot$ cm^{-4}, $k_2 = -22.53$ cm^{-1} and $k_3 = 8.65 \times 10^5$ dyne $\cdot$ cm^{-4}. The aim of this study is to understand how the size of the network, dependent on the level n_l of vessel ramifications, influences the aggregation process. For a given value of n_l, we construct then the network by adding the corresponding number n_b of bifurcations and the number n_a of arteries, Table 6 presents the values of n_l, n_a and n_b.

At the root of the network, the radius of the artery is $R_0 = 1$ cm and we impose the same pulsatile the flow rate (40) as in the previous section 5, with $Q_h = 100$ cm$^3 \cdot$ s^{-1} and $T_h = 1$ s. We also assume that blood enters the artery in a fully disaggregated state ($f = 0$). At the ends of each network we set as in the previous section a non-reflecting boundary conditions. We therefore detach ourselves from classical resistive boundary conditions and construct the network dynamics by adding successive levels of vessel ramifications. These boundary conditions are invariant with n_l and provide with the adequate framework to study network-size effects.

Finally, the initial conditions are (37) and the time- and space-discretization parameters of the network are described in Table 7. We present data obtained after 9 periods to ensure that the system has reached a periodic state.

6.1. Healthy network

We construct three healthy networks with $n_l \in \{2, 4, 6\}$. In Figure 7, we plot the distribution of the structure function f in the three networks at 4

n_l	n_b	n_a
2	3	7
4	15	31
6	63	127
n	$2^n - 1$	$2^{n+1} - 1$

Table 6: Number n_l of level of vessel ramifications, number n_b of bifurcations and number n_a of arteries of an idealized asymmetric network.

Δt [s]	Δx [cm]	Order
10^{-5}	10^{-2}	2

Table 7: Numerical parameters describing the time discretization and the mesh.

characteristic times of the last cardiac cycle: the beginning $t_1 = 9T_h$, the systolic peak $t_2 = 9.25T_h$, the middle $t_3 = 9.5T_h$ and the diastolic peak $t_4 = 9.75T_h$.

We observe clear effects of network size and asymmetry on the aggregation of RBCs. At $t = 9T_h$, the aggregation is high for $n_l = 2$, as the reflective behavior of the network is smaller due to the smaller number of bifurcations. At $t = 9.25T_h$, the inlet flow rate reaches its maximum value and blood is globally disaggregated for $n_l = \{2, 4, 6\}$. Nevertheless, for $n_l = 4$ and $n_l = 6$, aggregated regions remain in the left hand side (l.h.s.) large extremity arteries. These regions belong to high ramification levels and have not yet been reached by the incoming pulse wave. At $t = 9.5$, all RBCs have been disaggregated by the incoming pulse. Finally at $t = 9.75$, RBCs reaggregate in the l.h.s. large arteries since there is no flow coming from the heart and the reflected waves have been damped by viscous effects. Furthermore, the shear rate $\dot{\gamma}$ is lower in these larger arteries. Overall, aggregation dynamics depend on the size and asymmetry of the network and aggregation occurs principally in the large arteries of the l.h.s. and their immediate daughter arteries. In these arteries, the structure function reaches the critical value of $f \approx 0.1$, at which blood displays viscoelastic and thixotropic effects (see subsection 4.2).

These results indicate that we must take into account non-Newtonian ef-

fects in networks presenting large arteries or a high level of vessel ramifications. Furthermore, these results highlight the importance of vessel topology as the asymmetry of the network influences the aggregation dynamics.

6.2. Pathological network

In the literature, non-Newtonian blood effects have been particularly studied in elementary pathological networks such as bifurcations [59, 27, 24]. However, as observed before, the size and asymmetry of the network appears to play an important role in the aggregation dynamics. To characterize how pathologies can modify the blood flow and aggregation process in a large network, we introduce two severe stenoses of 90% of obstruction in the 3 networks. One stenose is located on the l.h.s., in the large radius branch of the network and the other is on the r.h.s, in the small radius branch. The exact position of both stenoses is represented in Figure 8 by circles ($\circ$).

As previously, we plot in Figure 8 the distribution of the structure function f over the three networks ($n_l \in \{2, 4, 6\}$) for the last cardiac cycle: $t_1 = 9T_h$, $t_2 = 9.25T_h$, $t_3 = 9.5T_h$ and $t_4 = 9.75T_h$. For $n_l \in \{4, 6\}$, the presence of the stenoses results in a higher blood aggregation in the arteries downstream of the stenoses compared to Figure 7. On the contrary for $n_l = 2$, the value of the structure f is lower than in Figure 7 as the stenoses create reflections that contribute to the disaggregation process. The results show that aggregation effects are amplified in pathological networks as the flow is reduced downstream of the stenoses. Upstream of the stenoses, aggregation is reduced due to additional reflected waves produced by the stenoses.

The numerical results presented in this section demonstrate that non-Newtonian behaviors exist in healthy and pathological networks. Even if these non-Newtonian behaviors are small, they are non-negligible. They affect in particular the WSS distribution in the networks, which plays an important role in cardiovascular pathogenesis. The non-Newtonian aspect of blood must therefore be taken into

account to accurately compute network hemodynamics, especially in pathological networks.

7. Conclusion

We have proposed a 1D generalized non-Newtonian blood flow model, based on a classical 1D approach for the conservation mass and the balance of momentum, but including time- and structure-dependent viscous effects. The evolution of the shear stress is governed by a Maxwell equation with coefficients depending on the state of aggregation of RBCs. The balance between aggregation and shear-dependent disaggregation is described by a kinetic equation, which is a particular case of a structural model for viscoelastic fluids [11, 15]. We note that this approach is not restricted to blood rheology and could be applied to other structured fluids.

We have confronted the numerical predictions of our 1D blood flow model to experimental data available in the literature [44, 14, 55], and we have shown that the model reproduces qualitatively and quantitatively the rheology of blood. We have further investigated the non-Newtonian effects in arterial networks of increasing size and demonstrated how the pulsatility of the flow and the network topology contribute to the aggregation process, which occurs mainly in the large arteries and their immediate daughter arteries. The aggregation of RBCs is further increased downstream of pathologies such as stenoses.

In the entire study, we have assumed, in a 1D framework, that the wall shear rate $\dot{\gamma}|_{r=R}$ solely contributes to the disaggregation process as structure is represented by a single homogeneous phase. The shear rate $\dot{\gamma}|_{r=R}$ therefore governs the evolution of the blood structure near the wall and in the bulk of the flow. In reality, the axial velocity profile varies with time and space leading to variations of $\dot{\gamma}$ along the radius of the artery. In particular, for axisymmetric flow, $\dot{\gamma}|_{r=0} = 0$. By using the wall shear rate $\dot{\gamma}|_{r=R}$ to govern the disaggregation process in the entire artery we have overestimated the shearing effects and therefore underestimated the non-Newtonian effects. However, we

have also assumed an *a priori* shape of the velocity profile, which is valid for experimental validation (see section 4) but an approximation for network flows. In sections 5 and 6, we have assumed a Poiseuille flow everywhere in the network, as is classically done in 1D applications, and therefore underestimated the value of $\dot{\gamma}$. To overcome those limitations due to the loss of the velocity profile in the 1D averaging process, we plan in future works to use the 2D multiring developed in [60] to compute the axial velocity profile and introduce radial variations in the aggregation process.

Keeping in mind these limitations inherent to the 1D framework, the 1D generalized non-Newtonian blood flow model presented here will be useful in the future to help understanding the hemodynamics in healthy and pathological networks of the micro- and macro-circulation.

References

[1] E. Marchandise, M. Willemet, V. Lacroix, A numerical hemodynamic tool for predictive vascular surgery, Medical engineering & physics 31 (1) (2009) 131–144.

[2] C. Audebert, P. Bucur, M. Bekheit, E. Vibert, I. E. Vignon-Clementel, J.-F. Gerbeau, Kinetic scheme for arterial and venous blood flow, and application to partial hepatectomy modeling, Computer Methods in Applied Mechanics and Engineering 314 (2017) 102–125.

[3] A. Ghigo, S. Abou Taam, X. Wang, P.-Y. Lagrée, J.-M. Fullana, A one-dimensional arterial network model for bypass graft assessment, Medical Engineering & Physics.

[4] P. J. Blanco, M. Pivello, S. Urquiza, R. Feijóo, On the potentialities of 3D–1D coupled models in hemodynamics simulations, Journal of Biomechanics 42 (7) (2009) 919–930.

[5] I. E. Vignon-Clementel, A. L. Marsden, J. A. Feinstein, A primer on com-

putational simulation in congenital heart disease for the clinician, Progress in Pediatric Cardiology 30 (1) (2010) 3–13.

[6] S. Sankaran, M. E. Moghadam, A. M. Kahn, E. E. Tseng, J. M. Guccione, A. L. Marsden, Patient-specific multiscale modeling of blood flow for coronary artery bypass graft surgery, Annals of biomedical engineering 40 (10) (2012) 2228–2242.

[7] F. Cuomo, S. Roccabianca, D. Dillon-Murphy, N. Xiao, J. D. Humphrey, C. A. Figueroa, Effects of age-associated regional changes in aortic stiffness on human hemodynamics revealed by computational modeling, PloS one 12 (3) (2017) e0173177.

[8] L. Formaggia, J.-F. Gerbeau, F. Nobile, A. Quarteroni, On the coupling of 3d and 1d navier–stokes equations for flow problems in compliant vessels, Computer Methods in Applied Mechanics and Engineering 191 (6) (2001) 561–582.

[9] P. Blanco, R. Feijóo, S. Urquiza, A unified variational approach for coupling 3D–1D models and its blood flow applications, Computer Methods in Applied Mechanics and Engineering 196 (41) (2007) 4391–4410.

[10] L. Formaggia, A. Quarteroni, C. Vergara, On the physical consistency between three-dimensional and one-dimensional models in haemodynamics, Journal of Computational Physics 244 (2013) 97–112.

[11] M. M. Cross, Rheology of non-newtonian fluids: a new flow equation for pseudoplastic systems, Journal of colloid science 20 (5) (1965) 417–437.

[12] G. B. Thurston, Viscoelasticity of human blood, Biophysical journal 12 (9) (1972) 1205–1217.

[13] G. B. Thurston, Elastic effects in pulsatile blood flow, Microvascular research 9 (2) (1975) 145–157.

[14] M. Bureau, J. Healy, D. Bourgoin, M. Joly, Rheological hysteresis of blood at low shear rate., Biorheology 17 (1-2) (1980) 191.

[15] D. Quemada, R. Droz, Blood viscoelasticity and thixotropy from stress formation and relaxation measurements: a unified model., Biorheology 20 (5) (1982) 635–651.

[16] C. Verdier, Review article: Rheological properties of living materials. from cells to tissues, Journal of Theoretical Medicine 5 (2) (2003) 67–91.

[17] Y. I. Cho, K. R. Kensey, Effects of the non-newtonian viscosity of blood on flows in a diseased arterial vessel. part 1: Steady flows, Biorheology 28 (3-4) (1991) 241–262.

[18] F. Yilmaz, M. Y. Gundogdu, et al., A critical review on blood flow in large arteries; relevance to blood rheology, viscosity models, and physiologic conditions, Korea-Australia Rheology Journal 20 (4) (2008) 197–211.

[19] A. J. Apostolidis, A. N. Beris, Modeling of the blood rheology in steady-state shear flows, Journal of Rheology 58 (3) (2014) 607–633.

[20] J. Bernsdorf, D. Wang, Non-newtonian blood flow simulation in cerebral aneurysms, Computers & Mathematics with Applications 58 (5) (2009) 1024–1029.

[21] F.-B. Tian, L. Zhu, P.-W. Fok, X.-Y. Lu, Simulation of a pulsatile non-newtonian flow past a stenosed 2d artery with atherosclerosis, Computers in biology and medicine 43 (9) (2013) 1098–1113.

[22] N. Nandakumar, K. C. Sahu, M. Anand, Pulsatile flow of a shear-thinning model for blood through a two-dimensional stenosed channel, European Journal of Mechanics-B/Fluids 49 (2015) 29–35.

[23] M. Jahangiri, M. Saghafian, M. R. Sadeghi, Numerical simulation of non-newtonian models effect on hemodynamic factors of pulsatile blood flow

in elastic stenosed artery, Journal of Mechanical Science and Technology 31 (2) (2017) 1003–1013.

[24] A. J. Apostolidis, A. P. Moyer, A. N. Beris, Non-newtonian effects in simulations of coronary arterial blood flow, Journal of Non-Newtonian Fluid Mechanics 233 (2016) 155–165.

[25] F. J. Gijsen, F. N. van de Vosse, J. Janssen, The influence of the non-newtonian properties of blood on the flow in large arteries: steady flow in a carotid bifurcation model, Journal of biomechanics 32 (6) (1999) 601–608.

[26] F. Gijsen, E. Allanic, F. Van de Vosse, J. Janssen, The influence of the non-newtonian properties of blood on the flow in large arteries: unsteady flow in a 90 curved tube, Journal of biomechanics 32 (7) (1999) 705–713.

[27] J. C. Weddell, J. Kwack, P. Imoukhuede, A. Masud, Hemodynamic analysis in an idealized artery tree: differences in wall shear stress between newtonian and non-newtonian blood models, PloS one 10 (4) (2015) e0124575.

[28] B. Moreau, B. Mauroy, Murray's law revisited: Quémada's fluid model and fractal trees, Journal of rheology 59 (6) (2015) 1419–1430.

[29] F. De Vita, M. de Tullio, R. Verzicco, Numerical simulation of the non-newtonian blood flow through a mechanical aortic valve, Theoretical and Computational Fluid Dynamics 30 (1-2) (2016) 129–138.

[30] R. B. Bird, Useful non-newtonian models, Annual Review of Fluid Mechanics 8 (1) (1976) 13–34.

[31] R. G. Owens, A new microstructure-based constitutive model for human blood, Journal of Non-Newtonian Fluid Mechanics 140 (1) (2006) 57–70.

[32] M. Moyers-Gonzalez, R. G. Owens, J. Fang, A non-homogeneous constitutive model for human blood. part 1. model derivation and steady flow, Journal of Fluid Mechanics 617 (2008) 327–354.

[33] K. Yeleswarapu, M. Kameneva, K. Rajagopal, J. Antaki, The flow of blood in tubes: theory and experiment, Mechanics Research Communications 25 (3) (1998) 257–262.

[34] M. Anand, K. Rajagopal, A shear-thinning viscoelastic fluid model for describing the flow of blood, Int. J. Cardiovasc. Med. Sci 4 (2) (2004) 59–68.

[35] M. Anand, J. Kwack, A. Masud, A new generalized oldroyd-b model for blood flow in complex geometries, International Journal of Engineering Science 72 (2013) 78–88.

[36] J. Fang, R. G. Owens, Numerical simulations of pulsatile blood flow using a new constitutive model, Biorheology 43 (5) (2006) 637–660.

[37] A. Duarte, A. I. Miranda, P. Oliveira, Numerical and analytical modeling of unsteady viscoelastic flows: The start-up and pulsating test case problems, Journal of Non-Newtonian Fluid Mechanics 154 (2) (2008) 153–169.

[38] M. A. Moyers-Gonzalez, R. G. Owens, J. Fang, A non-homogeneous constitutive model for human blood: Part iii. oscillatory flow, Journal of Non-Newtonian Fluid Mechanics 155 (3) (2008) 161–173.

[39] T. Bodnár, A. Sequeira, M. Prosi, On the shear-thinning and viscoelastic effects of blood flow under various flow rates, Applied Mathematics and Computation 217 (11) (2011) 5055–5067.

[40] P. Perdikaris, L. Grinberg, G. E. Karniadakis, An effective fractal-tree closure model for simulating blood flow in large arterial networks, Annals of biomedical engineering 43 (6) (2015) 1432–1442.

[41] T. Sochi, The flow of power law fluids in elastic networks and porous media, Computer methods in biomechanics and biomedical engineering 19 (3) (2016) 324–329.

[42] A. Pries, D. Neuhaus, P. Gaehtgens, Blood viscosity in tube flow: dependence on diameter and hematocrit, American Journal of Physiology-Heart and Circulatory Physiology 263 (6) (1992) H1770–H1778.

[43] A. J. Apostolidis, M. J. Armstrong, A. N. Beris, Modeling of human blood rheology in transient shear flows, Journal of Rheology 59 (1) (2015) 275–298.

[44] M. Bureau, J. Healy, D. Bourgoin, M. Joly, Etude rhéologique en régime transitoire de quelques échantillons de sangs humains artificiellement modifiés, Rheologica Acta 18 (6) (1979) 756–768.

[45] P. Sousa, J. Carneiro, R. Vaz, A. Cerejo, F. Pinho, M. Alves, M. Oliveira, Shear viscosity and nonlinear behavior of whole blood under large amplitude oscillatory shear, Biorheology 50 (5-6) (2013) 269–282.

[46] P.-Y. Lagrée, S. Lorthois, The rns/prandtl equations and their link with other asymptotic descriptions: application to the wall shear stress scaling in a constricted pipe, International Journal of Engineering Science 43 (3) (2005) 352–378.

[47] A. R. Ghigo, X.-F. Wang, R. Armentano, J.-M. Fullana, P.-Y. Lagrée, Linear and nonlinear viscoelastic arterial wall models: application on animals, Journal of Biomechanical Engineering 139 (1) (2017) 011003.

[48] S. Sherwin, L. Formaggia, J. Peiro, V. Franke, Computational modelling of 1D blood flow with variable mechanical properties and its application to the simulation of wave propagation in the human arterial system, International Journal for Numerical Methods in Fluids 43 (6-7) (2003) 673–700.

[49] X.-F. Wang, S. Nishi, M. Matsukawa, A. Ghigo, P.-Y. Lagrée, J.-M. Fullana, Fluid friction and wall viscosity of the 1d blood flow model, Journal of biomechanics 49 (4) (2016) 565–571.

[50] A. Ghigo, O. Delestre, J.-M. Fullana, P.-Y. Lagrée, Low-shapiro hydrostatic reconstruction technique for blood flow simulation in large arteries with

varying geometrical and mechanical properties, Journal of Computational Physics 331 (2017) 108–136.

[51] F. Bouchut, Nonlinear stability of finite Volume Methods for hyperbolic conservation laws: And Well-Balanced schemes for sources, Springer Science & Business Media, 2004.

[52] X. Wang, J.-M. Fullana, P.-Y. Lagrée, Verification and comparison of four numerical schemes for a 1D viscoelastic blood flow model, Computer methods in biomechanics and biomedical engineering 18 (15) (2015) 1704–1725.

[53] J. Murillo, P. García-Navarro, A Roe type energy balanced solver for 1D arterial blood flow and transport, Computers & Fluids 117 (2015) 149–167.

[54] H. Steffan, W. Brandstätter, G. Bachler, R. Pucher, Comparison of newtonian and non-newtonian blood flow in stenotic vessels using numerical simulation, in: Biofluid Mechanics, Springer, 1990, pp. 479–485.

[55] D. McMillan, J. Strigberger, N. Utterback, Rapidly recovered transient flow resistance: a newly discovered property of blood, American Journal of Physiology-Heart and Circulatory Physiology 253 (4) (1987) H919–H926.

[56] M. S. Olufsen, Structured tree outflow condition for blood flow in larger systemic arteries, American journal of physiology-Heart and circulatory physiology 276 (1) (1999) H257–H268.

[57] M. S. Olufsen, C. S. Peskin, W. Y. Kim, E. M. Pedersen, A. Nadim, J. Larsen, Numerical simulation and experimental validation of blood flow in arteries with structured-tree outflow conditions, Annals of biomedical engineering 28 (11) (2000) 1281–1299.

[58] P. J. Blanco, S. M. Watanabe, E. A. Dari, M. A. R. Passos, R. A. Feijóo, Blood flow distribution in an anatomically detailed arterial network model: criteria and algorithms, Biomechanics and modeling in mechanobiology 13 (6) (2014) 1303–1330.

[59] Y. Fan, W. Jiang, Y. Zou, J. Li, J. Chen, X. Deng, Numerical simulation of pulsatile non-newtonian flow in the carotid artery bifurcation, Acta Mechanica Sinica 25 (2) (2009) 249–255.

[60] A. Ghigo, J.-M. Fullana, P.-Y. Lagrée, A 2d nonlinear multiring model for blood flow in large elastic arteries, Submitted to the Journal of Computational Physics.

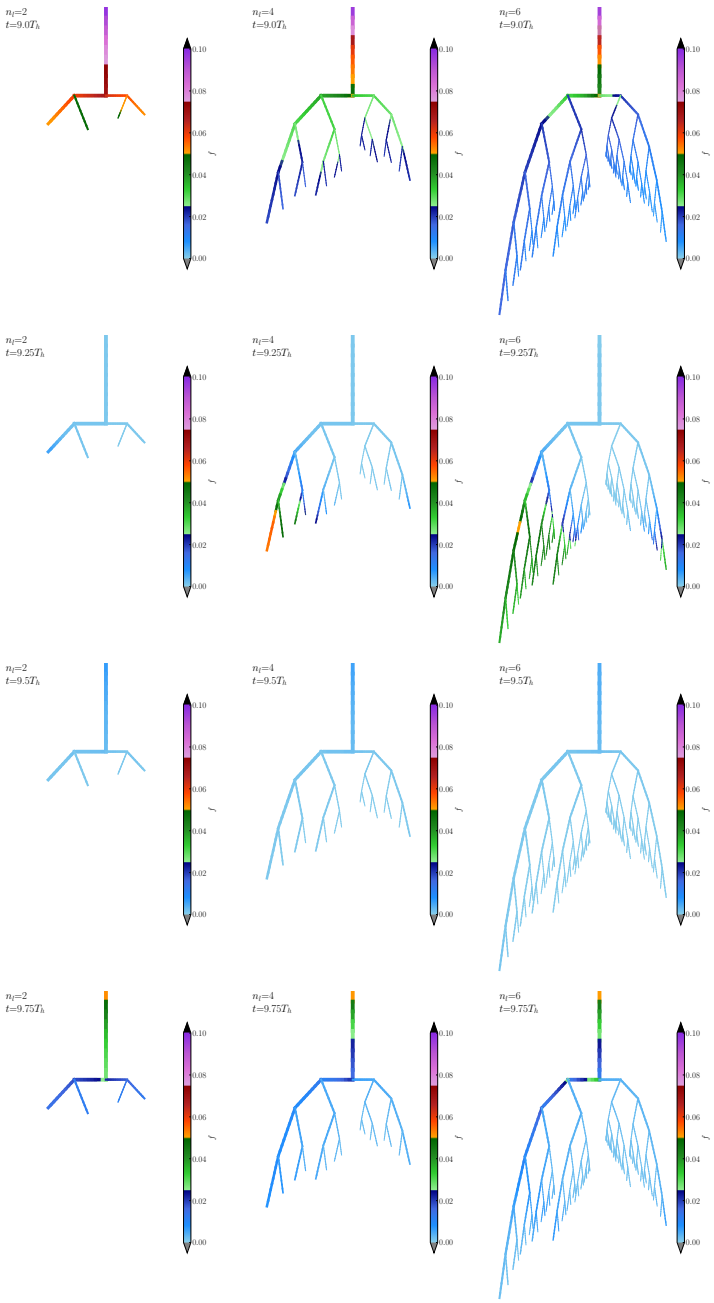

Figure 7: Snapshots at $t_1 = 9T_h$, $t_2 = 9.25T_h$, $t_3 = 9.5T_h$ and $t_4 = 9.75T_h$ of the distribution of the structure function f in three networks with increasing levels of ramification $n_l \in \{2 \text{ (left)}, 4 \text{ (middle)}, 6 \text{ (right)}, \}$. Aggregation occurs mainly in the large arteries on the l.h.s of the network and in their immediate daughter arteries. Aggregation depends on the pulsatility of the flow, the size and the asymmetry of the network.

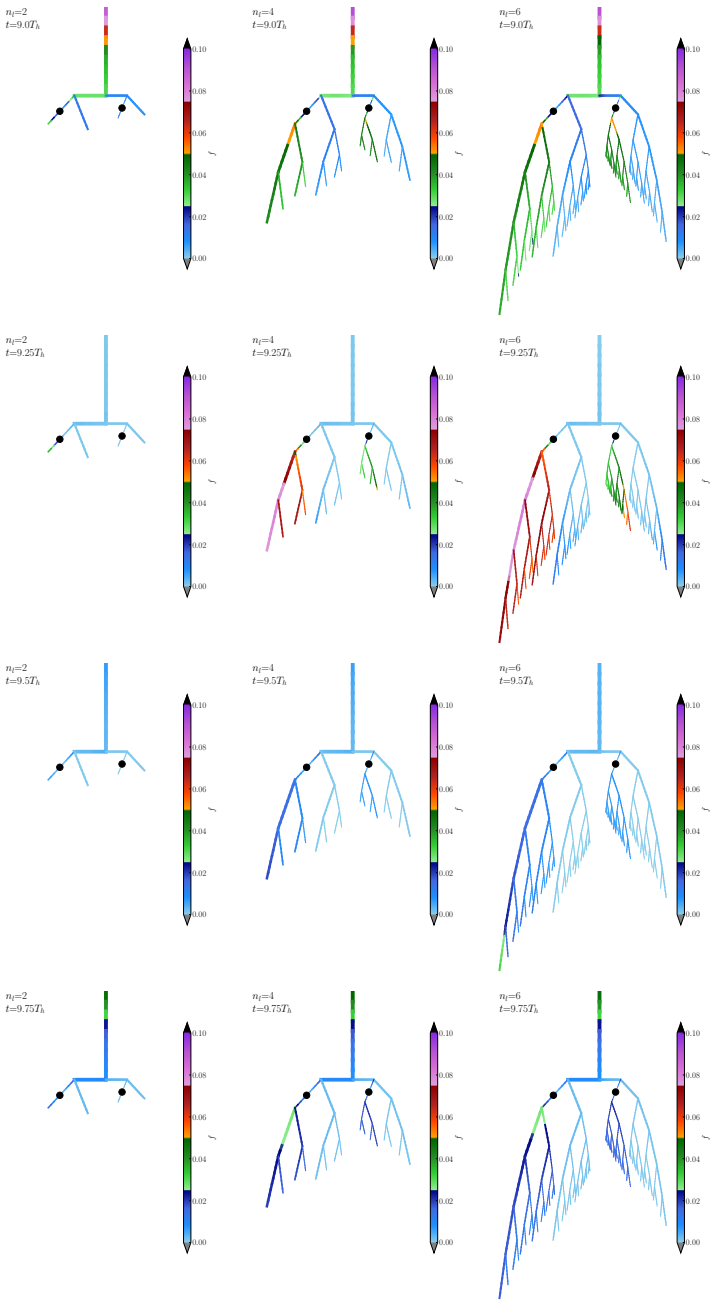

Figure 8: Snapshots at $t_1 = 9T_h$, $t_2 = 9.25T_h$, $t_3 = 9.5T_h$ and $t_4 = 9.75T_h$ of the distribution of the structure function f in three networks with increasing levels of ramification $n_l \in \{2 \text{ (left)}, 4 \text{ (middle)}, 6 \text{ (right)}, \}$, presenting two stenosis marked by the black circles ($\circ$). Aggregation now occurs in the large arteries on the l.h.s of the network and in their immediate daughter arteries but also on the r.h.s, downstream of the stenosis. In the arteries upstream of the stenoses, aggregation is reduced due to the additional reflections created by the stenoses.